Graphene Enhances Li Storage Capacity of Porous Single-Crystalline Silicon Nanowires

Xiao-Liang Wang and Wei-Qiang Han*

Center for Functional Nanomaterials, Brookhaven National Laboratory, Upton, New York 11973, United States

ABSTRACT We demonstrated that graphene significantly enhances the reversible capacity of porous silicon nanowires used as the anode in Li-ion batteries. We prepared our experimental nanomaterials, viz., graphene and porous single-crystalline silicon nanowires, respectively, using a liquid-phase graphite exfoliation method and an electroless HF/$AgNO_3$ etching process. The Si porous nanowire/graphene electrode realized a charge capacity of 2470 mAh g^{-1} that is much higher than the 1256 mAh g^{-1} of porous Si nanowire/C-black electrode and 6.6 times the theoretical capacity of commercial graphite. This relatively high capacity could originate from the favorable charge-transportation characteristics of the combination of graphene with the porous Si 1D nanostructure.

KEYWORDS: Li-ion battery • nanostructure • etching • electrode kinetics • anode

1. INTRODUCTION

The critical demand for high-energy, compact Li-ion batteries increasingly is driven by technologies such as clean transportation vehicles, space, and stationary power grids (1−3). One area of much interest presently is to find an alternative anode material with a Li storage capacity higher than that of graphite (372 mAh g^{-1}) that is the common commercial anode-material nowadays. Among the several candidates, silicon has garnered much research attention because it exhibits the highest known theoretical capacity, i.e., 4200 mAh g^{-1} (4−6).

The ultrahigh capacity of silicon stems from the fact that it exhibits electrochemical alloying storage behavior, unlike the insertion mechanism of graphite; ideally, $Li_{4.4}Si$ could form at the end of discharge. However, incorporating a huge amount of Li^+ inevitably causes gigantic changes in volume and, concomitantly, an intense lattice strain; consequently, particles are pulverized, and electrical connections are lost (4). Another practical limitation to the high performance of silicon comes from its semiconductive $\sim 10^{-5}$ S cm^{-1} charge transportation (compared with 10^3 S cm^{-1} of graphite) that hinders the electrode redox process and electronic diffusion.

In principle, several routes to accommodate the swing in volume and/or accelerate charge transfer within the electrode are feasible for enhancing the cell's performance. These ways include adding different carbon-conductive materials [e.g., carbon black (7), graphite (8), carbon nanotubes (9, 10), and graphenes (11, 12)], Si−C composites (6, 13), and different nanostructures [nanoparticles (14), nanowires (5, 15), nanotubes (16, 17), thin films (18), and nanopores (19)]. From the viewpoint of electronic conduction, graphene, a massless charge carrier with high mobility (200 000 cm^2 V^{-1} s^{-1}) (20, 21), is potentially the ultimate conductive additive for Li-ion batteries. Meanwhile, porous Si nanowires could better accommodate the changes in volume and mechanic strain because of their strain toleration (5) and many voids (19). Herein, we report the enhanced effect of graphene on the reversible capacity of Li-ion batteries using porous single-crystalline silicon nanowires as the anode materials.

2. EXPERIMENTAL METHODS

2.1. Chemicals. Graphite (powder, Aldrich), *N*,*N*-dimethylformamide (NMF, 99%, Aldrich), poly(*m*-phenylenevinylene-*co*-2,5-dictoxy-*p*-phenylenevinylene) (Aldrich), silicon wafer (Boron-doped, p-type, 0−100 Ω cm, (100), double-surface polished, University Wafer), hydrofluoric acid (HF, 48%, Aldrich), $AgNO_3$ (99+%, Aldrich), acetone (99.5% min., Mallinckrodt), isopropyl alcohol (99.5% min., Mallinckrodt), and nitric acid (HNO_3, 69% min., Aldrich) were used.

2.2. Preparation of Graphene. Graphene nanosheets were prepared by a liquid-phase exfoliation technique (22−24). Graphite powders were dispersed in a *N*,*N*-dimethylformamide (DMF) solution of poly(*m*-phenylenevinylene-*co*-2,5-dictoxy-*p*-phenylenevinylene) and sonicated to break them up into graphene nanosheets.

2.3. Preparation of Porous Silicon Nanowires. Si nanowires were obtained via an electroless etching process (25, 26), which involves etching p-type Si wafers in an aqueous mixture of HF and $AgNO_3$ via a nanoscale electrochemical $(Si + F^-)/Ag^+$ cell process. The Si wafers were cleaned by sequential sonication in acetone for 10 min and in isopropyl alcohol for 5 min. The surface oxidation layer was removed by further soaking the wafer in diluted HF (ca. 4%) for 10 min. Then, we immersed the wafer in a 0.04 M $AgNO_3$/5 M HF aqueous solution. The wafer, ~1 cm^2, was etched using a 5 mL solution for 2.5 h at room temperature. Next, the wafer was washed with water and further with HNO_3 to dissolve the deposited Ag deposition. The nanowires were collected via the doctor-blade methods.

2.4. Characterization. For nanostructural observations, we used a Hitachi S-4800 scanning electron microscope (SEM) and a JEM-2100F transmission electron microscope (TEM) with a field-emission gun and an energy dispersive X-ray spectroscopy (EDS) detector. The powder X-ray diffraction (XRD) experiment was carried out by a Rigaku/Miniflex II diffractometer with Cu Kα radiation. The electrode films for measuring cell performance consisted of silicon (nanowires or nanoparticles from Hefei, China), conductive additive (Graphene or Super-P carbon

* Corresponding author. E-mail: whan@bnl.gov.

Received for review September 9, 2010 and accepted November 15, 2010

DOI: 10.1021/am100857h

black from TIMCAL), and a binder [sodium carboxymethyl cellulose (CMC, $M_w \sim 90\,000$) from Aldrich]. The weight ratio of Si and carbon was 1:1, and the polymer binder was fixed to 10 wt % of the total weight. In the text, we used NP + CB, NW + CB, and NW + G to denote cells with Si nanoparticles/carbon black, Si nanowires/carbon black, and Si nanowires/graphene, respectively. Electrodes consist of 90 wt % carbon (graphene or carbon black), and 10 wt % sodium carboxymethyl cellulose were also prepared. Copper foils with surface treatment (0.025 mm thick, Schlenk) served as the current collector. For the fabrication of electrode films, Si, carbon, and the binder were blended with distilled water by magnetic stirring and sonication until a homogeneous slurry was formed, and then, the slurry was casted on Cu foils before drying. Water was evaporated under vacuum at room temperature, and the electrode films were further dried under vacuum at 110 □ for 8 h. The electrolyte solution was 1.0 M $LiPF_6$ in ethylene carbonate/dimethyl carbonate (1:1 by volume, purchased from Novolyte). A 20 μm polyolefin microporous membrane (Celgard 2320) was used as the separator. Laminated 2032-type coin cells with an electrode film/electrolyte-saturated separators/lithium foil (as the counter and reference electrode, 0.75 mm thick, 99.9% metal basis, Alfa) were fabricated inside an M. Braun LabMaster 130 glovebox under Ar atmosphere. The cell cycling was performed using an Arbin MSTAT system by a galvanostatic cycling procedure, with the current density of 105 mA g^{-1} (Si + C) between 0.005 and 0.8 V. The rate performance was measured between 0.1C and 2C [1C = 2100 mA g^{-1} (Si + C)] in the same voltage range, with the discharge rate fixed to 0.1C.

3. RESULTS AND DISCUSSION

Employing methods such as micromechanical exfoliation (27) and epitaxial growth (28) to prepare graphene results in sheets that are almost perfect crystallographically, but it is daunting to mass produce them. On the other hand, the reduction of graphite oxide produces gram-scale graphene but sacrifices the intact sp^2 hybridized bonds; accordingly, a large number of defects are left after reduction. Consequently, the charge transport behavior of graphene is suppressed significantly (29, 30). Therefore, we chose to employ the scalable, liquid-phase exfoliation of graphite to generate graphene that is unoxidized and has fewer defects. The carbon surface with fewer dangling bonds (like the case herein) may lead to the reduction in the Si−C interface strength, as suggested by Hertzberg et al. when they discussed the carbon coated Si tube (31). The interfacial contact between graphene and other materials could be mechanical and other types, such as physical or chemical interaction (32). We suggest that the mechanical contact is the main one.

Graphene nanosheets typically are micrometer-sized (Figure 1a). Figure 1b is a high-resolution TEM (HRTEM) image viewed of the single-crystalline graphene nanosheet along the [001] direction. Inset is a figure of the fast-Fourier-transform electron-diffraction patterns which also determines the character of the single-crystal. The fringes in the sheet are separated by about 0.34 nm, corresponding to that of the (002) plane of graphite crystal; the fringe contrast reflects the folding of the graphene sheet (23). Therefore, we can determine the number of layers based on the number of the fringes; in this image, there are five. Some graphene nanosheets have more than 10 layers.

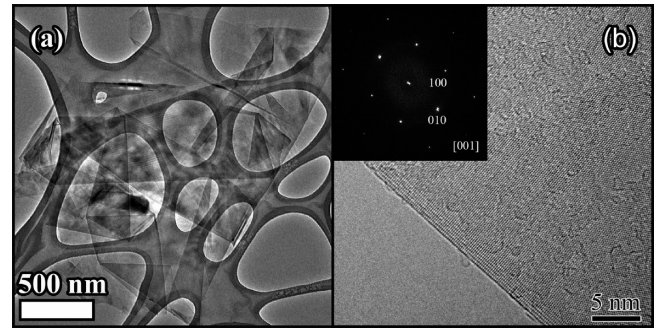

FIGURE 1. TEM images of graphene sheets. (a) Low magnification; (b) high magnification viewed along the [001] direction, where the inset shows the fast-Fourier-transform electron-diffraction patterns.

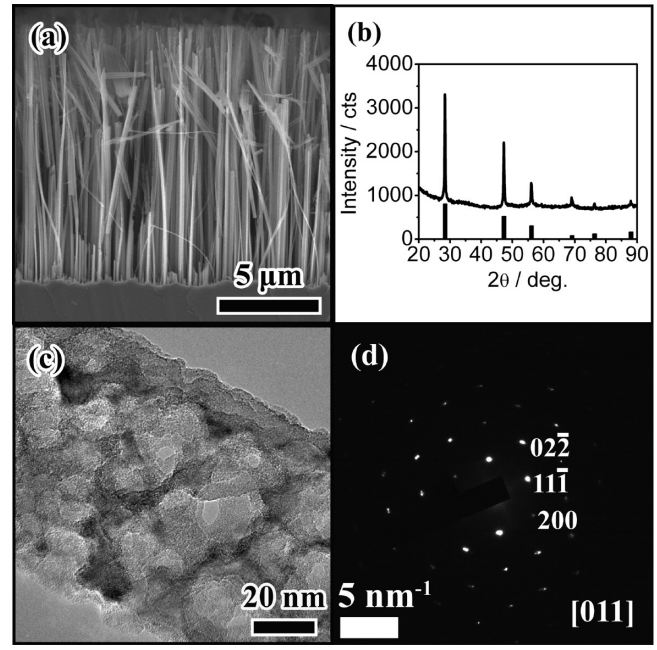

FIGURE 2. Porous single-crystalline Si nanowires. (a) SEM image of the wafer; (b) XRD patterns; (c) TEM image; and (d) SAED pattern along the [011] direction.

We obtained Si nanowires, 10 μm long, by electroless etching, as illustrated in Figure 2a. The XRD patterns shown in Figure 2b confirm the purity of the Si phase. TEM observations further revealed a highly porous nanostructure (Figure 2c). The pore size was ~5 nm, and the wall thickness was ~10 nm. Selected area electron diffraction (SAED) confirmed that the nanowires are single-crystalline ones (Figure 2d) with axial direction of ⟨100⟩.

The Si nanowires are formed via a nanoelectrochemical mechanism. Initially, the dissolution of Si and the deposition of dispersed Ag nanoclusters occur simultaneously under the following reaction (33):

$$4Ag^+ + Si + 6F^- \rightarrow 4Ag + SiF_6^{2-} \qquad (1)$$

Then, the continuous oxidation of silicon around the cathode Ag tips transfers electrons into Ag, upon which the corresponding reduction of Ag^+ occurs, and Ag dendrites grow. This process etches the wafer and results in the

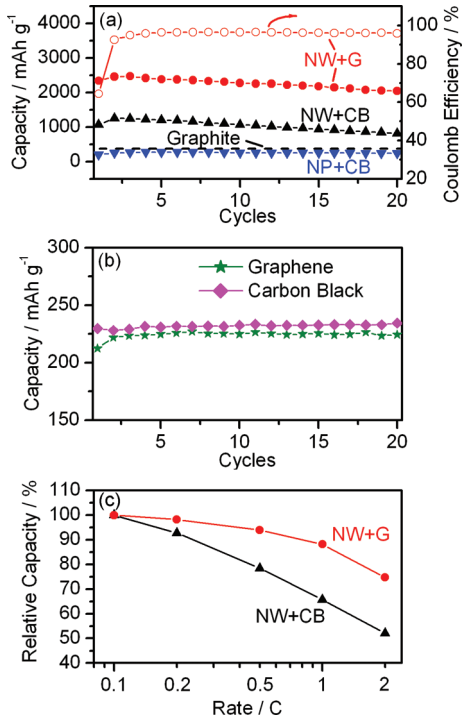

FIGURE 3. (a) Charge capacities and Coulomb efficiency of cells for 20 cycles. NW: Si nanowires; G: graphene; CB: carbon black; NP: Si nanoparticles. We removed the contribution to capacity from graphene and carbon black (b). (c) Rate capacities from 0.1C to 2C, with the rate for discharge fixed to 0.1C.

generation of nanowires. The favorable reaction dynamics of Ag/Ag^+ ensure the growth of the nanowires; the evolution of silver dendrites limits the merging of the nanoclusters by effectively absorbing any superfluous silver atoms that are deposited. Other metallic couplings, e.g., Pt/Pt^{4+} and Cu/Cu^{2+}, tend to form coalescent metal films on the wafer's surface that diminish the efficacy of etching (33).

Another important aspect of this etching process is the generation of pores. The surface roughness of the nanowires increases with declining resistivity, and finally, a porous structure appears in the wafer, in which the resistivity of Si wafers plays a decisive role. Novoselov et al. recorded the appearance of the porous structure when resistivity is <5 mΩ cm (26). The higher concentration of dopant atoms in wafers with higher conductivity seemingly facilitate pore formation by providing more nucleation spots and lowering the energy barrier for charge transfer. We were able to produce porous nanowires using wafers with much higher resistivity (<100 Ω cm) compared to those (<5 mΩ cm) used in the previous work (26). Furthermore, several factors, such as etching temperature and duration, $AgNO_3$ concentration, and the amount of etching solution, also may affect pore formation; e.g., etching in a 0.02 M $AgNO_3$ solution (1 cm^2 wafer vs ~2 mL solution) mainly results in dense nanowires.

Figure 3a shows the cell performances of porous silicon nanowires using conventional Super-P carbon black and graphene nanosheets as conductive additives. For comparison, we depict the reversible capacity of silicon nanoparticles, averaging 56 nm (determined from XRD). We removed most of the oxidized surface layer of nanoparticles by soaking them in diluted HF (ca. 4%) for 10 min before

Table 1. Cell Performance Data

electrode[a]	1st discharge capacity/mAh g^{-1}	1st charge capacity/mAh g^{-1}	Coulomb efficiency	Q20/Q1[b]
NP + CB	477	200	0.42	1.21
NW + CB	2172	1066	0.49	0.76
NW + G	3646	2347	0.64	0.87

[a] NW: Si nanowires; G: graphene; CB: carbon black; NP: Si nanoparticles. The capacity contribution from graphene or carbon black was removed (Figure 3b). [b] The ratio of charge capacity at the 20th cycle vs at the 1st cycle.

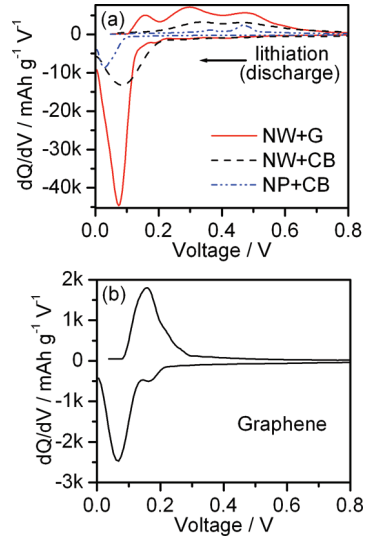

FIGURE 4. (a) Differential capacity dQ/dV curves of the first charge/discharge cycle. NW: Si nanowires; G: graphene; CB: carbon black; NP: Si nanoparticles. (b) Differential capacity dQ/dV curve of the first cycle of the graphene cell.

making the electrode membrane. The initial discharge and charge capacities of the silicon nanoparticles were, respectively, 477 and 200 mAh g^{-1}, with the Coulomb efficiency of 42%. Upon cycling, the capacity slightly increased to 274 mAh g^{-1} at the sixth cycle and, afterward, dropped slowly to 242 mAh g^{-1} at the 20th cycle. In contrast, a nanowire electrode with the same content of carbon black exhibited much higher initial capacities (Table 1) of about five times those of the nanoparticles, with an enhanced efficiency. Its reversible capacity decreased gradually upon cycling, after an enhancement to 1256 mAh g^{-1} at the second cycle; capacity at the 20th cycle was 815 mAh g^{-1}.

The enhanced capacity of porous Si nanowires is explainable by their highly accessible surfaces and short diffusion distance; thus, more Si sources are involved in the reaction with Li^+. Differential capacity curves (dQ/dV) verify the electrodes' kinetics. As illustrated in Figure 4a, for an NP + CB (Si nanoparticles/carbon black) cell, the onset voltage for the amorphous Li–Si alloy formation is ~0.1 V, and this crystalline Si-amorphous alloy transformation exhibits a typical one-peak profile (6, 34). On the other hand, the appearance of the Li–Si alloy in the NW + CB (Si nanowires/carbon black) sample begins at a higher voltage of ~0.22 V, indicative of a lower energy barrier for alloying and, thus, the resulting superior electrode redox reactivity. The enhanced reactivity of nanowires also is reflected in the subsequent delithiation process wherein both cells exhibit

two major peaks. We assigned these two peaks to the low-voltage delithiation (~0.35 V, $Li_{x'+x''}Si \rightarrow Li_{x'}Si + x''Li^+ + x''e^-$) and the high-voltage delithiation (~0.47 V, $Li_{x'}Si \rightarrow Si + x'Li^+ + x'e^-$) of amorphous Li–Si alloys; amorphous silicon forms at the end of this process (34, 35). The peaks of the NW + CB cell again are higher than those of the NP + CB cell, with the 0.34 V peak shifting to a lower voltage and becoming stronger than the ~0.47 V peak compared with the nanoparticle cell. Therefore, we conclude that in the NW + CB cell, $Li_{x'+x''}Si$ enriched with Li forms during lithiation, and more silicon participates in Li cycling. The starting voltage of the lithiation process in the NP + CB cell (0.1 V) is similar to that of micrometer-sized Si (34), while that of ~0.2 V has been observed in Si nanowires (35), porous Si (36), and Si–C composite (6). Therefore, we believe that those nanostructures that enhance the electrochemical activity may lead to the decrease of overpotential. Conductivity may also play an important role.

Introducing graphene nanosheets as conductive additives further improves the reversible capacity of Si nanowires, as illustrated in Figure 3a and listed in Table 1. The initial charge capacity of the NW + G (Si nanowires/graphene) cell is 2347 mAh g^{-1}, with an improvement in both Coulomb efficiency (64%) and the capacity retention (87% after 20 cycles). The capacity reaches 2470 mAh g^{-1} at the third cycle, and the value is 2041 mAh g^{-1} at the 20th cycle. The Coulomb efficiency stabilizes at about 96% after the third cycle. Using graphene also enhances the rate performance. Figure 3c shows that the 2C capacity of the NW + G cell is ~75% of the value at 0.1C, while the NW + CB cell only can retain ~52% of the capacity. However, graphene has limited improvement on enhancing the capacity of the Si nanoparticles; the capacity reaches around 300 mAh g^{-1} (10% increasing), with an initial Coulomb efficiency of 49% (17% increasing). This may indicate that these nanoparticles have intrinsically inferior electrochemical activity.

As reflected in the differential capacity curves (Figure 4a), the peak intensities of both the discharging and charging steps of the NW + G cell are higher than in the NW + CB system. The Li–Si alloying process begins at a similar voltage of ~0.22 V. There is an additional peak at ~0.13 V in the charging curve of the NW + G sample that we assigned to the delithiation process of graphene (cf. Figure 4b).

This significant enhancement by graphene of the reversible capacity of the Si nanowires might reflect (1) graphene's extraordinary high charge conductivity and (2) the nanosheet's morphology that facilitates its interaction with Si nanowire. Since carbon black already is a relatively good electrical conductor and because electronic conductivity does not solely determine the kinetics of the electrode reaction, capacity enhancement by factor 1 might be limited. On the other hand, the graphene nanosheets cover large areas of the nanowires, i.e., affording greater areas of contact for charge transfer and, thus, facilitating the electrode reaction. In comparison, carbon black nanoparticles mainly offer "contacting points" with the nanowires (cf. Figure 5).

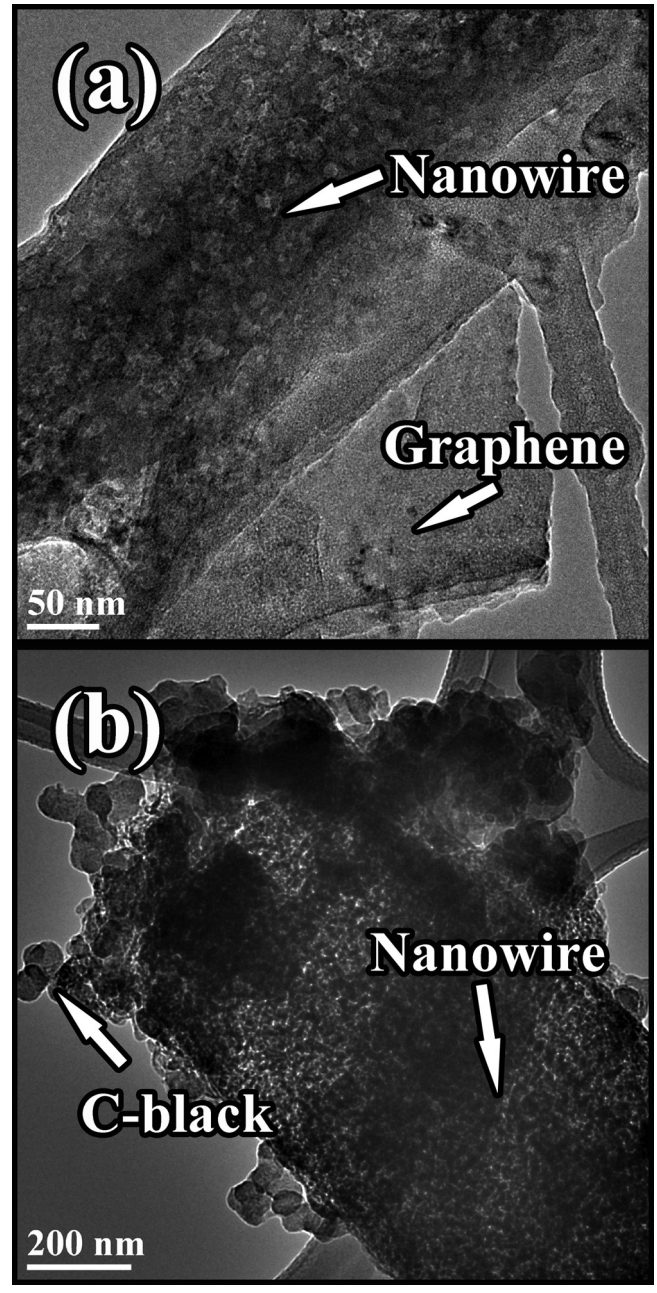

FIGURE 5. TEM images of Si nanowires after cycling: (a) the NW + G cell; (b) the NW + CB cell.

4. CONCLUSIONS

We prepared graphene nanosheets via scalable, liquid-phase exfoliation of graphite and fabricated porous single-crystalline silicon nanowires using an electroless etching protocol, employing an $HF/AgNO_3$ solution as the medium. As anodes in Li-ion batteries, Si nanowire electrodes possess higher reversible capacities than do Si nanoparticles. Introducing graphene nanosheets as the conductive additives rather than commercial carbon black further improves the electrochemical reactivity of Si nanowires. We recorded a reversible capacity of 2470 mAh g^{-1} in our porous Si nanowire/graphene system. Our results demonstrate the favorable charge-transmitting role of graphene and the beneficial kinetics-facilitating and nanostructure-stabilizing role of the porous nanowires.

Acknowledgment. This work is supported by the U.S. DOE under Contract DE-AC02-98CH10886 and E-LDRD Fund of Brookhaven National Laboratory. We thank Drs. Chao Ma and Lihua Zhang for their technical help and valuable discussions.

REFERENCES AND NOTES

(1) Armand, M.; Tarascon, J. M. *Nature* **2008**, *451*, 652–657.
(2) Li, H.; Wang, Z. X.; Chen, L. Q.; Huang, X. J. *Adv. Mater.* **2009**, *21*, 4593–4607.
(3) Goodenough, J. B.; Kim, Y. *Chem. Mater.* **2010**, *22*, 587–603.
(4) Kasavajjula, U.; Wang, C. S.; Appleby, A. J. *J. Power Sources* **2007**, *163*, 1003–1039.
(5) Chan, C. K.; Peng, H. L.; Liu, G.; McIlwrath, K.; Zhang, X. F.; Huggins, R. A.; Cui, Y. *Nat. Nanotechnol.* **2008**, *3*, 31–35.
(6) Magasinski, A.; Dixon, P.; Hertzberg, B.; Kvit, A.; Ayala, J.; Yushin, G. *Nat. Mater.* **2010**, *9*, 353–358.
(7) Li, H.; Huang, X. J.; Chen, L. Q.; Wu, Z. G.; Liang, Y. *Electrochem. Solid State Lett.* **1999**, *2*, 547–549.
(8) Liu, W. R.; Guo, Z. Z.; Young, W. S.; Shieh, D. T.; Wu, H. C.; Yang, M. H.; Wu, N. L. *J. Power Sources* **2005**, *140*, 139–144.
(9) Chan, C. K.; Patel, R. N.; O'Connell, M. J.; Korgel, B. A.; Cui, Y. *ACS Nano* **2010**, *4*, 1443–1450.
(10) Wang, W.; Kumta, P. N. *ACS Nano* **2010**, *4*, 2233–2241.
(11) Lee, J. K.; Smith, K. B.; Hayner, C. M.; Kung, H. H. *Chem. Commun.* **2010**, *46*, 2025–2027.
(12) Chou, S. L.; Wang, J. Z.; Choucair, M.; Liu, H. K.; Stride, J. A.; Dou, S. X. *Electrochem. Commun.* **2010**, *12*, 303–306.
(13) Hu, Y. S.; Adelhelm, P.; Smarsly, B. M.; Maier, J. *ChemSusChem* **2010**, *3*, 231–235.
(14) Kim, H.; Seo, M.; Park, M. H.; Cho, J. *Angew. Chem., Int. Ed.* **2010**, *49*, 2146–2149.
(15) Huang, R.; Fan, X.; Shen, W. C.; Zhu, J. *Appl. Phys. Lett.* **2009**, *95*, 133119.
(16) Park, M. H.; Kim, M. G.; Joo, J.; Kim, K.; Kim, J.; Ahn, S.; Cui, Y.; Cho, J. *Nano Lett.* **2009**, *9*, 3844–3847.
(17) Song, T.; Xia, J. L.; Lee, J. H.; Lee, D. H.; Kwon, M. S.; Choi, J. M.; Wu, J.; Doo, S. K.; Chang, H.; Il Park, W.; Zang, D. S.; Kim, H.; Huang, Y. G.; Hwang, K. C.; Rogers, J. A.; Paik, U. *Nano Lett.* **2010**, *10*, 1710–1716.
(18) Maranchi, J. P.; Hepp, A. F.; Kumta, P. N. *Electrochem. Solid State Lett.* **2003**, *6*, A198–A201.
(19) Kim, H.; Han, B.; Choo, J.; Cho, J. *Angew. Chem., Int. Ed.* **2008**, *47*, 10151–10154.
(20) Bolotin, K. I.; Sikes, K. J.; Jiang, Z.; Klima, M.; Fudenberg, G.; Hone, J.; Kim, P.; Stormer, H. L. *Solid State Commun.* **2008**, *146*, 351–355.
(21) Fuhrer, M. S.; Lau, C. N.; MacDonald, A. H. *MRS Bull.* **2010**, *35*, 289–295.
(22) Li, X. L.; Wang, X. R.; Zhang, L.; Lee, S. W.; Dai, H. J. *Science* **2008**, *319*, 1229–1232.
(23) Han, W. Q.; Wu, L. J.; Zhu, Y. M.; Watanabe, K.; Taniguchi, T. *Appl. Phys. Lett.* **2008**, *93*, 223103.
(24) Hernandez, Y.; Nicolosi, V.; Lotya, M.; Blighe, F. M.; Sun, Z. Y.; De, S.; McGovern, I. T.; Holland, B.; Byrne, M.; Gun'ko, Y. K.; Boland, J. J.; Niraj, P.; Duesberg, G.; Krishnamurthy, S.; Goodhue, R.; Hutchison, J.; Scardaci, V.; Ferrari, A. C.; Coleman, J. N. *Nat. Nanotechnol.* **2008**, *3*, 563–568.
(25) Peng, K. Q.; Yan, Y. J.; Gao, S. P.; Zhu, J. *Adv. Mater.* **2002**, *14*, 1164–1167.
(26) Hochbaum, A. I.; Gargas, D.; Hwang, Y. J.; Yang, P. D. *Nano Lett.* **2009**, *9*, 3550–3554.
(27) Novoselov, K. S.; Jiang, D.; Schedin, F.; Booth, T. J.; Khotkevich, V. V.; Morozov, S. V.; Geim, A. K. *Proc. Natl. Acad. Sci. U.S.A.* **2005**, *102*, 10451–10453.
(28) Sutter, P. W.; Flege, J. I.; Sutter, E. A. *Nat. Mater.* **2008**, *7*, 406–411.
(29) Eda, G.; Fanchini, G.; Chhowalla, M. *Nat. Nanotechnol.* **2008**, *3*, 270–274.
(30) Park, S.; Ruoff, R. S. *Nat. Nanotechnol.* **2009**, *4*, 217–224.
(31) Hertzberg, B.; Alexeev, A.; Yushin, G. *J. Am. Chem. Soc.* **2010**, *132*, 8548–8549.
(32) Williams, G.; Seger, B.; Kamat, P. V. *ACS Nano* **2008**, *2*, 1487–1491.
(33) Peng, K. Q.; Yan, Y. J.; Gao, S. P.; Zhu, J. *Adv. Funct. Mater.* **2003**, *13*, 127–132.
(34) Obrovac, M. N.; Krause, L. J. *J. Electrochem. Soc.* **2007**, *154*, A103–A108.
(35) Chan, C. K.; Ruffo, R.; Hong, S. S.; Huggins, R. A.; Cui, Y. *J. Power Sources* **2009**, *189*, 34–39.
(36) Kim, H.; Cho, J. *Nano Lett.* **2008**, *8*, 3688–3691.

AM100857H